Effects of continental emissions on Cloud Condensation Nuclei (CCN) activity in northern South China Sea during summertime 2018

Mingfu Cai[1,2,4], Baoling Liang[1], Qibin Sun[1], Shengzhen Zhou[1,5], Bin Yuan[4], Min Shao[4], Haobo Tan[2*], and Jun Zhao[1,3,5*]

[1] School of Atmospheric Sciences, Guangdong Province Key Laboratory for Climate Change and Natural Disaster Studies, and Institute of Earth Climate and Environment System, Sun Yat-sen University, Guangzhou, Guangdong 510275, China

[2] Institute of Tropical and Marine Meteorology/Guangdong Provincial Key Laboratory of Regional Numerical Weather Prediction, CMA, Guangzhou, Guangdong 510640, China

[3] Southern Laboratory of Ocean Science and Engineering (Guangdong, Zhuhai), Zhuhai, Guangdong, 519082, China

[4] Institute for Environmental and Climate Research, Jinan University, Guangzhou, Guangdong 511443, China

[5] Guangdong Provincial Observation and Research Station for Climate Environment and Air Quality Change in the Pearl River Estuary, Guangzhou, Guangdong 510275, China

Corresponding authors: Jun Zhao (zhaojun23@mail.sysu.edu.cn) and Haobo Tan (hbtan@gd121.cn)

Abstract. Aerosol particles in marine atmosphere have been shown to significantly affect cloud formation, atmospheric optical properties, and climate change. However, high temporal and spatial resolved atmospheric measurements over sea are currently sparse, limiting our understanding of aerosol properties in marine atmosphere. In this study, a ship-based cruise campaign was conducted over northern South China Sea (SCS) region (19°37′ N to 22°43′ N, 113°44′ E to 118°12′ E) during summertime 2018. Chemical compositions of the non-refractory PM_1 (NR-PM_1), particle number size distribution (PNSD) and size-resolved cloud condensation nuclei (CCN) activity (at supersaturation

Atmospheric
Chemistry
and Physics
Discussions

27   SS=0.18%, 0.34%, and 0.59%) were measured by a time-of-flight aerosol chemical speciation monitor

28   (ToF-ACSM), and the combination of a cloud condensation nuclei counter (CCNc) and a scanning

29   mobility particle sizer (SMPS), respectively. Overall, aerosol particles exhibited a unimodal

30   distribution (centering at 60~80 nm) and dominated by sulfate (~46%) in the NR-PM$_1$, similar to the

31   characteristic of previously-reported background marine aerosols. Two polluted episodes were

32   respectively observed at the beginning (P1, 6th-8th August) and at the end (P2, 25th-26th August) of the

33   campaign and both were characterized by high particle number concentrations (N$_{CN}$) which were

34   shown to originate from local emissions or pollutants from long range transport. Two relatively clean

35   periods (C1, 9th-10th and C2, 19th-21st August) prior to and after tropical storm Bebinca (11th-15th

36   August) were also classified due to substantial removal of pollutants by strong winds and rainfalls

37   accompanying with the storm. A value of about 0.4 for aerosol hygroscopicity parameter κ measured in

38   this study falls in a range of values (i.e., 0.2-1.0) reported previously for urban atmosphere and for

39   remote marine atmosphere.

40   The concentrations of trace gases (i.e., O$_3$, CO, NO$_X$) and particles (N$_{CN}$ and N$_{CCN}$ at SS=0.34%) were

41   elevated at the end of the campaign and decreased with the offshore distance, suggesting important

42   impacts of anthropogenic emissions from the inland Pearl River Delta (PRD) region on the northern

43   SCS. A good correlation between NO$_X$ concentration and N$_{CN}$ implies similar sources (e.g., heavy ship,

44   traffic, and biomass burning) for NOx and particles. The results showed that the N$_{CCN}$/N$_{CN,tot}$ and the κ

45   values obtained from the CCNc measurement (SS=0.34%) had no clear correlation either with the

46   offshore distance or with the concentrations of the particles. Back trajectory analysis showed that the

47   air pollutants originated from local emissions and from inland China continent via long range transport

48   during P1 and P2, respectively. In addition, the air was affected by air masses from southwest and from

49   Indo-China Peninsula during the clean C1 and C2 periods respectively. Chemical composition

50   measurements showed an increase of organic mass fraction and no obviously different κ values were

51   obtained from CCN measurements during C2 and P2, implying that the air masses carried pollutants

52   from local sources during long range transport from Indo-China Peninsula and from the inland China

53   continent respectively during the above two periods. Our study highlights dynamical variations of

54   particle properties and the impact of long range transport from the China continent and Indo-China

55   Peninsula on the northern SCS region during summertime.

56

57 **1   Introduction**

58   Aerosol particles directly affect global radiation balance by scattering and absorbing solar

59 radiation. Meanwhile, they can alter cloud microphysics, lifetime, and albedo, indirectly affecting heat

60 transfer through atmosphere (Stocker, 2013). However, high uncertainties still exist on their

61 contributions to the climatic impact, partly owing to our limited knowledge on spatial and temporal

62 distribution of aerosol particles and their properties in various environments. Thus, it is essential to

63 conduct field measurements under different environments to obtain chemical and physical properties of

64 particles, including chemical composition, particle number size distribution (PNSD), and cloud

65 condensation nuclei (CCN) activity, in order to better understand the radiation forcing induced by

66 aerosol particles.

67   The CCN activity describes how particles grow into cloud droplets and further affect cloud

68 development. Whether particles can be activated as CCN is determined by their chemical composition,

69 hygroscopicity, size, and ambient supersaturation (SS). Generally, the CCN activity can be described

70 by Köhler theory based on the water activity in solution, surface tension, molecular weight of water,

71 temperature, and diameter of the particle (Köhler, 1936). Alternatively, the hygroscopicity parameter κ

72 proposed by Petters and Kreidenweis (2007) can be used to characterize the CCN activity. Aerosol

73 hygroscopicity describes the ability of particles to grow by absorbing moisture in ambient

74 environments. The κ values can be measured in subsaturation (RH<100%) condition by the

75 hygroscopicity-tandem differential mobility analyzer (HTDMA) measurements or in supersaturation

76 (RH>100%) by the cloud condensation nuclei counter (CCNc) measurements.

77   Field measurements for the CCN activity have been conducted primarily in terrestrial

78 environments (e.g., urban cities, forested areas, and remote countryside areas) (Rose et al., 2010; Wang

79   et al., 2010; Cerully et al., 2011; Pierce et al., 2012; Hong et al., 2014; Cai et al., 2018). Cerully et al.

80   (2011) reported κ values ranging from 0.1 to 0.4 in forest during the 2007 EUCAARI campaign and

81   concluded that the κ values obtained from the HTDMA measurements were generally 30% lower than

82   those from the CCNc measurements. Wang et al. (2010) showed that the mixing state of particles was

83   important in predicting the CCN number concentration (N_{CCN}). Cai et al. (2018) found that the CCN

84   activity increased by decreasing the surface tension through increase of organic fractions in particles

85   based on the measurements of the CCN activity, hygroscopicity, and chemical composition in the Pearl

86   River Delta (PRD) region. Progresses on the aforementioned field measurements conducted in the

87   continental environments have substantially improved our understanding of the influence of aerosols in

88   global radiation forcing and precipitation under the terrestrial environments.

89   Aerosol particles in the marine atmosphere, on the other hand, have been well known to

90   significantly affect cloud development, atmospheric optical properties, and climate change (Johnson et

91   al., 2004; Ackerman et al., 2004; Mulcahy et al., 2008). Fewer field measurements were conducted in

92   the oceanic atmosphere than those in land, leading to less characterization of marine aerosol particles.

93   Remote sensing and ship-based cruise methods are two typical approaches employed to measure

94   aerosol properties in marine environments (Durkee et al., 1986; Kim et al., 2009; Lehahn et al., 2010;

95   Huang et al., 2018). Compared to ship-based measurements, remote sensing covers spatially a larger

96   area and temporally a longer period which are essential in the characterization of marine aerosols. For

97   example, Reid et al. (2013) employed remote sensing to describe long range transport patterns in the

98   Southeast Asia. The aerosol size information was compared between the retrievals from Moderate

99   Resolution Imaging Spectroradiometer (MODIS) and the measurements from ground-based

100   radiometers such as Aerosol Robotic Network (AERONET) over ocean (Kleidman et al., 2005).

101 However, extensive cloud coverages over oceanic region can significantly affect the quality and

102 availability of satellite measurements. Furthermore, dry bias or clear-sky bias also challenge satellite

103 measurements for obtaining accurate data (John et al., 2011; Reid et al., 2013; Choi and Ghim, 2017).

104 Moreover, remote sensing using satellite sensors is limited in providing high time resolution (i.e.,

105 minutes), high spatial resolution (i.e., within tens of meters in dimension) data and specific particle

106 properties (i.e., hygroscopicity and chemical composition). Although ship-based measurements are

107 limited in spatial coverage, they can provide higher spatial and temporal resolution for obtaining

108 comprehensive physical and chemical properties of gas and aerosol particles. Huang et al. (2018)

109 measured chemical composition of particles with a high-resolution time-of-flight aerosol mass

110 spectrometer (HR-ToF-AMS) over the Atlantic Ocean aboard a campaign ship and found that about 19%

111 of organics originated from continental long-range transport. Kim et al. (2009) found that particle size

112 distribution varied in a dynamic range, depending on the meteorological conditions over the Yellow

113 Sea and the East China Sea. Atwood et al. (2017) showed that biomass burning, anthropogenic

114 pollution from continent and ship emissions would affect the remote South China Sea during the

115 southwestern monsoon (SWM) season. However, few ship-based campaigns are available in the

116 literature on measurements of atmospheric composition including gases and aerosol particles,

117 especially in several important China sea regions (e.g., SCS).

118   The air over northern SCS is affected by anthropogenic pollution from the adjacent Pearl River

119 Delta region, China inner continent, and Indo-China Peninsula (Zhang et al., 2018). Furthermore, as

120 one of the most important and busy trading regions in China, the PRD and the northern SCS are

121 subjected to severe air pollution due to emissions from heavy loadings of cargo ships and fishing

122 vessels (Lv et al., 2018). Special weather patterns are dominant in the SCS during summertime which

123   are characterized by southwest monsoon (SWM) and occasionally affected by typhoons. Typically,

124   typhoon brings heavy precipitation and strong wind to this region, which helps to remove air pollutants.

125   However, on one hand, it has been found that downdrafts prior to a typhoon usually affect negatively

126   atmospheric diffusion, leading to the accumulation of the air pollutants in the region (Feng et al., 2007).

127   On the other hand, marine background particles and emissions from Indo-China Peninsula are brought

128   into this region through SWM. As a result, the physical and chemical properties of marine aerosol

129   particles vary dynamically which can be distinguished from those of continental particles. Differences

130   (i.e., physical and chemical properties, life cycle) between the two types of aerosol particles reflect

131   different transport pathways and source origins which are not well known. In addition, lack of

132   understanding on aerosol characteristics will inevitably hinder our ability to evaluate the impacts of

133   aerosol particles on global radiation forcing and atmospheric processes. Thus, ship-based field

134   measurements are urgently needed in this region in order to understand the CCN activity, chemical

135   composition, particle size distribution, and their relationships with continental and marine air masses.

136   In this study, we report results from a recent ship-based cruise measurement in the northern SCS

137   during summertime 2018. During the campaign, size-resolved CCN activity, chemical composition,

138   and particle number size distribution were measured by a CCNc, a time-of-flight aerosol chemical

139   speciation monitor (ToF-ACSM) and a scanning mobility particle sizer (SMPS), respectively. Temporal

140   and spatial distributions of the aerosol chemical and physical properties and impact of different air

141   masses on the properties were investigated. Our results provide valuable knowledge on the effects of

142   long range transport and on the atmospheric processes in the SCS.

143

144 **2   Methodology**

145 **2.1   Ship-based campaign**

146   The cruise campaign is a routine comprehensive exercise organized by Sun Yat-sen University

147 (SYSU) during summertime 2018 (6th to 27th August) including a variety of multidisciplinary sciences

148 (i.e., atmosphere, ocean, chemistry, geology, and biology). The round-trip journey both started and

149 ended at Huizhou port (22°43′ N, 114°36′ E) which is about 140 km from Guangzhou, traveling

150 towards northern SCS with an area between 19°37′ N to 22°43′ N and 113°44′ E to 118°12′ E. The ship

151 track includes two routes during which the vessel was anchored near the port due to tropical storm

152 Bebinca as its track was shown in Fig. 1a, along with the complete, color-coded ship track. The first

153 route started 7th August from the port and arrived northeast of Dongsha Islands (20°45′ N 118°12′ E) on

154 10th August 2018, and then returned to anchor near the port during the typhoon period (11th to 15th

155 August). The second route left the port on 15th August toward Hong Kong and arrived at its south in the

156 afternoon (18:00 local time, LT). The vessel then headed southeast for about 42 hours on 18th August

157 and turned toward Dongsha Islands. It anchored at several sites around this sea area and then returned

158 on 24th August following a similar pathway as the first route to Huizhou port on 27th August.

159   A commercial vessel with a capacity of 8000 ton was employed for the routine summer

160 measurement campaign whose schematic diagram was shown in Fig. 1b. An air conditioned (T=298K)

161 sea container of about 30 m^2 housed all the instruments which was listed in Table 1 and was placed in

162 the front deck of the vessel. Trace gases, including O_3, SO_2, CO, NO_X (NO and NO_2), were measured

163 by gas analyzers (model T400U, T100U, T300, and T200U, Teledyne API Inc., USA, respectively).

164 Detailed descriptions of the major instruments used in the campaign could be found in the following

Atmospheric
Chemistry
and Physics
Discussions

165   subsection. The aerosol sampling port with a PM$_{2.5}$ cyclone inlet was made of a 5 m long 3/8″ o.d.

166   stainless-steel tube which extended outside of the container with an inclination angle of 45 °to the deck.

167   The inlet is about 2.5 m above the deck and 1.5 m away from the container. All aerosol sampling flows

168   firstly passed through a Nafion dryer (model MD-700, Perma Pure Inc., USA) to reach a relative

169   humidity (RH) lower than 30%. The gas sample inlet made of a 2 m long 1/4″ o.d. Teflon tube with a

170   similar inclination angle, also extended outside of the container. For consistency, any abnormal data

171   were removed from the dataset, including either abnormal particle number size distribution or spike

172   high number concentrations of particles (measured by SMPS), organics (measured by ToF-ACSM), and

173   NO$_X$ (measured by the NO$_X$ monitor) which were most likably from emissions of the vessel or other

174   neighbor ships.

175

176   **2.2 Origins of air masses by HYSPLIT**

177   The Hybrid Single-Particle Lagrangian Integrated Trajectory (HYSPLIT) model developed by

178   National Oceanic and Atmospheric Administration (NOAA) was used to investigate trajectories of air

179   movement for identification of source origins which might affect the northern SCS region during the

180   campaign. The model calculated the 72 hours back trajectories of air masses at 6 hours intervals

181   arriving at the campaign vessel. The arrival height of the trajectories was set to be 150 m, 500 m, and

182   1000 m above the ground level, a reasonable representative of the air masses. The Global Data

183   Assimilation System (GDAS) 1 °× 1 °meteorological data was employed to drive the HYSPLIT.

184

185   **2.3 Measurements**

186   **2.3.1 Size-resolved cloud condensation nuclei activity**

187   The size-resolved CCN activity was measured with combination of a homemade scanning

188   mobility particle sizer system and a cloud condensation nuclei counter (model CCNc-200, DMT Inc.,

189   USA). The homemade SMPS system consisted of a differential mobility analyzer (DMA, model 3081L,

190   TSI., Inc.) and a condensation particle counter (CPC, model 3787, TSI Inc.). The CCNc-200 has two

191   parallel cloud columns (column A and B) which measure the CCN concentrations (N_{CCN}) at two

192   specific SS at the same time. Only the N_{CCN} measured by column A was discussed in this study. During

193   the measurements, the SMPS system was operated in a scanning mode. The sample particles after the

194   Nafion dryer were firstly neutralized by a X-ray neutralizer (model 3088, TSI., Inc., USA) and were

195   subsequently classified by the DMA. The selected particles were split into the CPC for measurements

196   of total particle number concentration (with a flow rate of 0.6 LPM) and the CCNc for measurements

197   of the CCN number concentration at a specific supersaturation (with a flow rate of 0.5 LPM). The

198   SMPS and the CCNc system were set to measure particle number size distribution and size-resolved

199   CCN number concentration at a mobility size range of 10-400 nm. The supersaturation of the CCNc

200   was set to be 0.18%, 0.34%, and 0.59%. Before the measurements, the CCNc-200 was calibrated with

201   ammonium sulfate ((NH_4)$_2SO_4$) particles at three SS (0.18%, 0.34%, and 0.59%), detailed description

202   of the calibration could be found in Cai et al. (2018). The SMPS system was also calibrated with

203   standard polystyrene latex spheres (PSL, with a size of 20 nm, 50 nm, and 200 nm) prior to the

204   campaign.

205

206   **2.3.2 Aerosol chemical composition**

207   An Aerodyne time-of-flight aerosol chemical speciation monitor was deployed to measure bulk

208   non-refectory PM_1 chemical composition during the campaign. The ToF-ACSM can provide mass

209   concentration of sulfate, nitrate, ammonium, chloride, and organics, except non-refectory components

210   such as sea salt, black carbon, and crustal species. Detailed description of ToF-ACSM can be found in

211   Fröhlich et al. (2013) and only a brief introduction relevant to this work was given here. During the

212   campaign, the measurement cycle of the ToF-ACSM was set to be about 10 min and the mass resolving

213   power was about 160. The sample flow dried by the Nafion dryer firstly entered an automatic

214   three-way valve, of which one way was directly connected to the lens system and the other way was

215   connected to a filter before entering the aerodynamic lens. By switching the automatic valve

216   periodically, the instrument can measure the total signal without a filter and the background signal with

217   a filter, thus the net signal representing the chemical composition of the aerosol particles can be

218   obtained. The aerodynamic lens system removes particles larger than 1 μm (at aerodynamic diameter,

219   D_{VA}) and has a relative low transmission for small particles ($D_{VA} < 50$ nm). Monodisperse pure

220   ammonium nitrate (NH_4NO_3) and ammonium sulfate ($(NH_4)_2SO_4$) particles generated by a homemade

221   atomizer and then selected by a DMA (about 300 nm in diameter) were used to calibrate the relative

222   ionization efficiency (RIE) value of NH_4 (RIE_{NH_4}) and SO_4 (RIE_{SO_4}) at the beginning and at the end of

223   the campaign.

224

225   **2.4   Data processing of CCN activation**

226   The size-resolved N_{CN} and N_{CCN} measured by the SMPS and CCNc-200 system was used to

227   calculate the activation ratio (AR), which was defined as the ratio of N_{CCN} to N_{CN} at each size bin. The

228   size-resolved ARs were inverted based on the method described by Moore et al. (2010). The AR

229   spectrum was then fitted using a three-parameter fit:

230    $$\frac{N_{CCN}}{N_{CN}} = \frac{B}{1+(\frac{D_p}{D_{50}})^C} \; ,$$ (1)

231   where D_p represents dry particle diameter (nm), B, C and D_{50} are the three fitting parameters which

232   represent the asymptote, the slope, and the inflection point of the sigmoid, respectively (Moore et al.,

233   2010). The D_{50} is called the critical diameter, where 50% of the particles are activated at a specific SS.

234   A hygroscopicity parameter κ which represents the CCN activity was calculated from the critical

235   saturation ratio (Sc) and D_{50} from the following equation (Petters and Kreidenweis, 2007):

236    $$\kappa = \frac{4A^3}{27D_{50}^3(\ln Sc)^2} \; , \quad A = \frac{4\sigma_{s/a}M_w}{RT\rho_w} \quad ,$$ (2)

237   where ρ_w is density of pure water (about 997.04 kg m^{-3} at 298.15K), M_w is molecular weight of water

238   (0.018 kg mol^{-1}), $\sigma_{s/a}$ is surface tension of the solution/air interface which is assumed to be value of

239   pure water ($\sigma_{s/a}$ =0.0728 N m^{-1} at 298.15K), R is the universal gas constant (8.314 J mol^{-1} K^{-1}), T is

240   thermodynamic temperature in Kelvin (298.15K), and D_{50} is the critical diameter (in meter).

241

242   **3   Results and Discussion**

243   **3.1 Overview**

244   Figure 2 shows number size distribution (a), mass concentration and fraction (b and c), number

245   concentration of CCN (d), and hygroscopicity parameter (e) measured by different instruments during

246   the campaign. The particle sizes were predominantly larger than 10 nm, implying that no new particle

247   formation events were observed during the campaign. Furthermore, the distribution exhibited mainly

248 unimodal characteristics which peaked at a size range of about 60-80 nm. The average number

249 concentration was about 3400 cm^{-3}, which was in general lower than that in inland PRD region (Cai et

250 al., 2017) and slightly lower than the ship measurement (4335 cm^{-3}) over the East China Sea (Kim et al.,

251 2009). However, two relative polluted periods were classified with high particle number concentrations

252 at the beginning (6th-8th August, defined as P1 with a particle size peaking at about 80 nm) and at the

253 end (25th-26th August, defined as P2 peaking at about 100 nm) of the campaign. In contrast, two

254 relatively clean periods were identified in between (9th-10th August, defined as C1 and 19th-21st August,

255 defined as C2).

256   Temporal profile of the mass concentration (Fig. 2a) measured by ToF-ACSM was consistent with

257 that of PNSD, which showed the highest concentration on 25th August. The total measured mas

258 concentration of NR-PM$_1$ varied dramatically from 0.92 to 85.08 μg m^{-3}, with a median of 7.97 μg m^{-3}.

259 Mass concentrations of PM$_{2.5}$ were reported over the same region during Cruise I (27.6 μg m^{-3}) and

260 Cruise II (10.10 μg m^{-3}) in Zhang et al. (2007). The mass concentration in our measurements was

261 higher than that in clean marine atmosphere (from 0.27 to 1.05 μg m^{-3}) reported at the coastal station,

262 Ireland (Ovadnevaite et al., 2014) and the atmosphere over the Atlantic Ocean (Huang et al., 2018).

263 Mass concentration of SO_4^{2-} varied from 0.35 to 33.20 μg m^{-3}, with a median of 3.66 μg m^{-3}, which

264 falls in a range of previous measurement in Dongsha Islands (1.3 to 5.5 μg m^{-3}, Chuang et al., 2013).

265 The average mass fraction of NR-PM$_1$ during the campaign was dominated by sulfate (46%), followed

266 by organics (35%), ammonium (14%), nitrate (3%), and chloride (2%), which was similar to the

267 measurement over the Atlantic Ocean (Huang et al., 2018). The chemical composition over northern

268 SCS was quite different from that at the urban site which was dominated by organics largely from

269 anthropogenic sources (Cai et al., 2017). A higher mass fraction of sulfate in the marine atmosphere

Atmospheric
Chemistry
and Physics
Discussions

270   may probably be attributed to nearby ship emissions rather than oxidation of dimethyl sulfide (DMS)

271   emitted from the ocean. However, solid evidences are needed since the emission inventory in the

272   northern SCS region is still lacking and the sources of sulfate in this region remain currently unknown.

273   The number concentrations of CCN (N_{CCN} at SS=0.18%, 0.34%, and 0.59%) and total particles

274   (N_{CN}) were shown in Fig. 2d. The N_{CN} values during the two polluted periods (P1 and P2) were

275   significantly higher than the average N_{CN} (3463 cm^{-3}) over the whole campaign period and those from

276   other marine measurements (Cai et al., 2017; Kim et al., 2009). This average value falls between the

277   smoke type (2280 cm^{-3}) and the port type (4890 cm^{-3}) measured over the remote South China Sea

278   (Atwood et al., 2017). Note that since the abnormally spiked signals which were probably caused by

279   emissions of the nearby ships or the ship itself were removed in the data processes, the high N_{CN} values

280   during those episodes were likely attributed to regional pollution or long range transport from

281   continents. In general, the N_{CCN} values at the three supersaturations increased with increase of the N_{CN}.

282   The average value of N_{CCN} (1544 cm^{-3}, SS=0.34%) fell in the range of the simulated values (1000-2000

283   cm^{-3}, SS=0.4%) reported in a previous study (Yu and Luo, 2009), suggesting that the model employed

284   in the study in general successfully predicted the N_{CCN} in the SCS region. Although the N_{CCN} and N_{CN}

285   were relatively higher in P1 and P2 than the average value, they remained overall low during the

286   campaign compared to those from the inland PRD sites. The N_{CCN} values in P1 were lower than those

287   in P2 with similar values of N_{CN} in both P1 and P2, suggesting a lower activation fraction in P1 than in

288   P2, which cloud be attributed to relatively high fractions of smaller particles and a lower hygroscopcity

289   in P1. As discussed above, particles peaked at a smaller size in P1, leading to fewer particles larger than

290   D_{50}. The time series of the κ values calculated using Eq. 2 show that the aerosol hygroscopicity was

291   lower at the beginning of the campaign, leading to a lower CCN activity in P1. The measurements

292   could be affected by local fresh emissions with lower hygroscopic particles in urban since the ship was

293   anchored near Huizhou port and Hong Kong during P1, similar to lower hygroscopicity for urban

294   particles previously measured by Cai et al. (2017). Furthermore, low particle hygroscopicity was found

295   from 11th August to 15th August when the ship was sheltered at the port from the tropical storm

296   Bebinca.

297   Aerosol hygroscopicity, an important parameter affecting CCN activity, can vary largely in its

298   values under different environments due to a variety of particle sources (Adam et al., 2012; Liu et al.,

299   2014; Hong et al., 2014; Wu et al., 2013; Cai et al., 2017). Comparison of the hygroscopicity parameter

300   κ obtained from this study, from urban Guangzhou, from remote marine Okinawa, remote South China

301   Sea, and mountain Goldlauter was shown in Fig. 3. The κ_{median} values obtained from this study (around

302   0.4) fall between those at the continental sites (Guangzhou and Goldlauter) and remote marine

303   measurement (remote South China Sea and Okinawa) and are barely dependent on particle sizes whose

304   pattern is quite similar to those in Okinawa. Moreover, a κ value was respectively reported to be in a

305   range of 0.22-0.65 measured by CCNc over the remote South China Sea and in a range of 0.30-0.56

306   measured by HTDMA over the coast of central California during a flight campaign (Atwood et al.,

307   2017; Hersey er al., 2009). In addition, high hygroscopicity values (0.56-1.04) measured by HTDMA

308   were also reported over the Pacific and Southern Oceans (Berg et al., 1998). In contrast to maritime

309   environments (i.e., SCS and Okinawa), the κ_{median} values in Guangzhou (0.21-0.31) are much lower and

310   increase obviously with particle sizes. The low hygroscopicity for small particles in Guangzhou was

311   attributed to local emissions from traffic and industry (Cai et al., 2017). The cruise in this campaign is

312   in an offshore region where the air is affected by anthropogenic emissions from the adjacent inland

313   PRD region, leading to medium values of aerosol hygroscopicity between urban and marine

314   background regions.

3.2 Temporal and spatial distributions

316   As discussed above, the air over the offshore northern SCS is affected by local emissions from

317   inland PRD regions. The shoreline along Huizhou port is roughly 45° inclined to the latitude (from

318   South to North) and it is reasonable to assume that the concentrations of the air pollutants originating

319   from local emissions are generally dependent on the distance offshore which can be roughly

320   represented by the latitude in this study. Hence in this section, the temporal and spatial concentration

321   distributions of air pollutants (particles and gases) were presented with latitude and the dates were

322   color-coded, representing from the beginning (dark blue) to the end (dark red) of the cruise (Fig. 4).

323   The concentrations of trace gases (O_3, CO, and NO_X), N_{CN}, and N_{CCN} (SS=0.34%) were higher during

324   the late half than during early half of the campaign, while SO_2 concentration varied in an opposite way,

325   suggesting that the sources of the air pollutants or the air masses were different at the beginning and at

326   the ending of the campaign. In particular, the aforementioned quantities increased substantially with

327   latitude (the higher the latitude the closer to the shore) from 19th to 26th August, indicating that the air

328   masses from inland China could affect the northern SCS region during this period. However, the

329    $N_{CCN}/N_{CN,tot}$ and κ values (SS=0.34%) showed almost no pattern (Figs. 4g and 4h), except that the

330    $N_{CCN}/N_{CN,tot}$ values were both high (about 0.8) at the beginning and at the end of the cruise. The

331    $N_{CCN}/N_{CN,tot}$ was defined as the ratio of number concentration of cloud condensation nuclei and total

332   aerosol particles at a specific SS. The κ values were observed to be relatively low when the vessel

333   located at a latitude of about 22 °N corresponding to 6th and 26th August, suggesting that the air was

334   affected by local fresh emissions which increased the organic content of the particles. Interestingly, a

335 higher value on 26th August than on 6th August was clearly shown (Fig. 4g) due probably to larger

336 averaged particle sizes on 26th August (about 110 nm) which were more easily activated than smaller

337 particles on 6th August (about 60-90 nm).

338   To further investigate the effects of local emissions on aerosol particles over northern SCS, the

339 correlations of SO_2, CO, NOx concentration, N_{CCN}, $N_{CCN}/N_{CN,tot}$, κ with N_{CN} were explored (Fig. 5).

340 The variation of SO_2 concentration was independent on N_{CN}, suggesting that SO_2 did not likably

341 originate from the same source as particles. In comparison, CO concentration was correlated with N_{CN}

342 during the second half of the cruise, implying that CO might share the same source as particles. An

343 excellent correlation between NOx concentration and N_{CN} was shown in all ranges of particle number

344 concentrations, implying that the aerosol particles might originate from the same source as NOx which

345 was likably attributed to traffic and industry in the continental PRD region. The N_{CCN} was observed to

346 follow two distinct trends for the first and second half of the cruise which show in general a higher

347 activation efficiency during the second half of the campaign, especially when N_{CN} is greater than about

348 7000 cm^{-3}, further validated by a much higher $N_{CCN}/N_{CN,tot}$ ratio against N_{CN} as shown in Fig. 5e. As

349 discussed in the previous paragraph, distinct κ values were seen at the very beginning and at the end of

350 the campaign, suggesting that the properties and sources of the particles could be different as will be

351 further discussed in the case study below.

352 **3.3 Case Study**

353   In section 3.1, we classified four periods (all in August) based upon particle number concentration,

354 corresponding to P1 (6th to 8th), C1 (9th to 10th), C2 (19th to 21st), and P2 (25th to 26th) as shown in Fig. 6.

355 During the two clean periods (C1, before Bebinca; C2, after Bebinca), the vessel travelled around

356 northeast of Dongsha islands where the particle number concentrations remained relatively low which

357   were not affected by the continental emissions from the PRD region. However, high number

358   concentrations of particles were observed during P1 when the vessel was close to the shore where the

359   air was substantially affected by local emissions from either Hongkong or Huizhou. During the last two

360   days in P2, even higher particle number concentrations were observed, suggesting that the pollutants

361   might originate from inland continent via long range transport.

362   We performed HYSPLIT to investigate the source origins of the air pollutants according to

363   movement of air masses during the campaign (Fig. 7). The backward trajectories during P1 showed that

364   the air masses were mainly from east and south and when arriving at the location of the vessel, the air

365   masses were stagnant on the shore, suggesting that the pollutants might originate from local emissions.

366   Interestingly, particle number concentrations were low during 11th to 15th August when the vessel was

367   sheltered from Bebinca, due probably to the arrival of the typhoon which caused high wind speeds and

368   brought rainfall in the northern SCS, resulting in removal of air pollutants in Huizhou and in Hong

369   Kong. The air masses over northern SCS originated from southwest (C1) or from Indo-China Peninsula

370   (C2) due to summer monsoon during the two clean periods (Fig. 7). The air masses moved northerly

371   during P2 and brought high concentrations of particles from inland China to PRD region, and then

372   further to the northern SCS (Fig. 7).

373   Chemical speciation by ToF-ACSM showed that the mass fractions of aerosol composition were

374   substantially different during C1, C2, and P2, except for nitrate whose fraction remain almost constant

375   among the above three periods (Fig. 8). Note that the mass fraction during P1 was not available for

376   comparison due to instrumental failure. Even the mass fractions during the two clean periods were

377   distinctly different, in particular, those of organics (26% for C1 vs 40% for C2), ammonium (19% for

378   C1 vs 12% for C2), and chloride (7% for C1 vs 2% for C2), although the particle composition was

379   dominated by sulfate which was almost equal in mass fraction (44% for C1 vs 42% for C2). The mass

380   fraction during C1 was dominated by sulfate, followed by organics, ammonium which was similar to

381   that in remote marine region (Cai et al., 2017). The mass fraction of sulfate in the NR-PM$_1$ during C1

382   and C2 was also similar to the previous study (44% and 43% in PM$_{2.5}$ for Cruise I and II, respectively)

383   over the northern SCS (Zhang et al., 2007). Although the mass fraction was still dominated by sulfate, a

384   substantially increasing fraction of organic (increase of 26% for C1 to 40% for C2) was observed. This

385   increase in organic fraction was likably attributed to the air masses passing through Indo-China

386   Peninsula which brought significant local sources. In contrast to the clean periods, the mass fraction in

387   the NR-PM$_1$ during P2 was dominated by organics (47%), followed by sulfate (33%) and ammonium

388   (13%), similar to that in urban areas (Huang et al., 2014), indicating that air masses from the north

389   could bring continental particles in inland China to the northern SCS.

390   The particle number size distribution (PNSD) was measured by the custom-made SMPS which

391   was described in the methodology section. The average particle number concentrations during P1 and

392   P2 (9239 and 10088 cm^{-3} respectively) were much higher than those during the clean periods (1826 and

393   1683 cm^{-3} for C1 and C2 respectively). In addition, the PNSD during the pollution periods was

394   characterized by an obvious accumulation mode that was attributed to secondary aerosols (Fig. 9),

395   while the one during the clean periods has a smaller and a less obvious accumulation mode and a more

396   obvious Aitken mode which was more related to marine background particles (Cai et al., 2017; Atwood

397   et al., 2017; Kim et al., 2009). The median diameters and concentration of the accumulation mode

398   during C1 and C2 was similar to those previously reported in South China Sea (Reid et al., 2015). Note

399   that the fitted nucleation modes for both clean and pollution periods were barely seen due to the

400   obviously low concentrations of particles in this mode. The lognormal median diameters for the Aitken

401   mode (70.4 nm) and the accumulation mode (165.7 nm) during P2 were respectively larger than those

402   (48.6 nm and 143.1 nm) during P1, implying more aging processes and particle growth in the long

403   range transport from the inland continent. Furthermore, a wider accumulation mode during C2 than

404   during C1 was observed, implying more complex sources for larger size particles which could probably

405   be attributed to biomass burning or anthropogenic activities across Indo-China Peninsula.

406   The CCN activity parameters (average N_{CCN}, D_{50}, and $N_{CCN}/N_{CN,tot}$ at SS=0.18%, 0.34%, and

407   0.59%) during each period were summarized in Table 2. Note that the N_{CCN} values (SS=0.34%) during

408   P1 and P2 (3969 and 7139 cm^{-3}) were much higher than the simulated values (1000-2000 cm^{-3},

409   SS=0.4%) (Yu and Luo, 2009) since the modeled CCN concentrations represent averaged values in a

410   larger regional scale than those measured in our ship-based cruise study. It also implied that the

411   continental emissions had significant impact on the CCN concentrations in the SCS region. Although

412   the mass fractions of chemical composition for C1, C2, and P2 were quite different among those

413   periods, no significant differences of the CCN activity parameters were seen, indicating particles with a

414   size range of 30-120 nm were less affected by long range transport from Indo-China Peninsula or

415   inland China continent. The calculated median κ values based on the measured D_{50} ranged from 0.32 to

416   0.41 and no significant differences in diameters and periods were observed (Fig. S1), suggesting that

417   the high mass fractions of organics during C2 might be distributed in larger particle size (Fig. 8). The

418   D_{50} values during P2 were smaller at all supersaturation ratios, suggesting higher hygroscopicity and

419   CCN activity during this period. In addition, the $N_{CCN}/N_{CN,tot}$ and N_{CCN} during P2 was larger than

420   during P1, owing to a larger number fraction of accumulation mode and a higher hygroscopicity.

421   Meanwhile, the median κ values fell in a range of 0.12-0.19 during P1, significantly lower than those

422   during three other periods but similar to the values measured in urban cities (Tan et al., 2013; Jiang et

Atmospheric
Chemistry
and Physics
Discussions

423   al., 2016; Cai et al., 2018). Such lower values of hygroscopicity were probably contributed from local

424   emissions originating from inland urban cities or heavy duty ships. More cruise campaigns are hence

425   needed to identify the source origins of marine aerosols over the SCS region.

426

427   **4   Conclusions**

428   As an annual routine exercise for SCS expedition during summertime, the 2018 cruise campaign

429   organized by Sun Yat-sen University is a comprehensive and interdisciplinary field measurement

430   involving atmosphere, ocean, geology, biology, and chemistry etc. The measurement includes

431   stationary and navigating observations based on compromise among multiple disciplines. For

432   atmospheric measurements, several key scientific questions are emerging to be addressed over SCS

433   region, including sources of air pollutants (gases and particles) in marine atmosphere, impacts of

434   biomass burning from southeastern Asia and summer monsoon on atmospheric chemistry and physics

435   in SCS region. In this study, the CCN activity, chemical composition, and particle number size

436   distribution over northern SCS were measured using several onboard instruments including a

437   TOF-ACSM, a CCNc, a SMPS, several monitors for trace gases (i.e., SO_2, NO_X, CO, and O_3), and

438   offline high flow particle collectors. On one hand, lower concentrations of key trace gas pollutants and

439   particle number or mass were observed in atmosphere of SCS than those in urban areas in PRD region,

440   consistent with previously reported values for background marine atmosphere. Overall, chemical

441   composition of NR-PM_1 was dominated by sulfate (46%) and the PNSD showed bimodal distribution

442   centering at ~80 nm and the hygroscopicity κ values being higher than those in urban areas. On the

443   other hand, characteristics of air pollutants (e.g., concentrations, physical and chemical properties)

21

444   show substantially variations during summer monsoon season, depending on source origins.

445   Characteristics similar to continental aerosols were shown when air masses originate from inland China

446   continent or Indo-China peninsula possibly via long range transport, leading to increase of organic

447   fraction in chemical composition and decrease of hygroscopicity which might be attributed to picking

448   up locally emitted and fresh pollutants during transport. Furthermore, low hygroscopicity κ values were

449   also shown when the air was affected by local fresh emissions and in this case the number

450   concentration of particles increased with decrease of offshore distance. In addition, concentrations of

451   both NOx and CCN concentrations were well correlated with the total concentration of particles.

452   Interestingly, a tropical storm Bebinca was caught in the middle of the campaign, resulting in two

453   relatively clean periods (C1 and C2). These clean periods were likably attributed to strong wind and

454   rainfall brought by the typhoon which could obviously blow away or wash out pollutants in northern

455   SCS region.

456   Our results suggest that aerosol properties and trace gases concentration over northern SCS is

457   complex and substantially variable. The median hygroscopicity κ values of the particles in northern

458   SCS were measured to be about 0.4, in the range of between those in the remote northwestern Pacific

459   Ocean and those in urban PRD region, implying that particles in northern SCS could be a mixture of

460   marine background and anthropogenic particles from continents (e.g., Indo-China peninsula and inland

461   China continent). Concentrations of aerosol particles and trace gases exhibit complex temporal and

462   spatial distribution. Concentrations of trace gases (i.e., O_3, CO, and NO_X except SO_2), particles (i.e.,

463   N_{CN} and N_{CCN}) were higher at the beginning (pollution episode: P1) than at the end (pollution episode:

464   P2) of the campaign, implying different source origins for the two periods. At the beginning of the

465   campaign, the air was likely affected by local fresh emissions from Huizhou, leading to increase of

Atmospheric
Chemistry
and Physics
Discussions

466   concentrations of both measured trace gases (except SO_2) and particles with decrease of offshore

467   distance. Meanwhile, concentration of NO_X had a good correlation with the N_{CN}, suggesting they might

468   originate from the same sources. Similarly, at the end of the campaign, concentrations of both

469   measured trace gases (except SO_2) and particles also increased with decrease of offshore distance,

470   while because of more larger particles, higher fractions of particles were activated at the end than at the

471   beginning of the campaign. We attributed the source origin during this period to inland China content

472   via long range transport with additional local fresh pollutants during transport process, leading to

473   barely clear patterns for both $N_{CCN}/N_{CN,tot}$ and D_{50} at all applied SS (SS=0.18, 0.34, and 0.59%).

474   Furthermore, our results indicate that biomass burning from southeastern Asia may have important

475   impacts on chemical composition and properties of aerosol particles over northern SCS, in particular,

476   leading to increase of organic mass fractions and decrease of hygroscopicity κ values and hence

477   affecting CCN activity in the region. Our study highlights the necessity for performing more intensive

478   ship-based atmospheric measurements in order to better understand marine aerosols and air pollution in

479   SCS region.

480

481   *Data availability.* Data from the ship-based cruise measurements are available upon request (Jun Zhao

482   via zhaojun23@mail.sysu.edu.cn).

483

484   *Supplement.* The supplement related to this article is available online at xxx.

485

486   *Author contributions.* **MC, JZ,** and **HT** designed the research. **MC** and **BL** performed the ship-based

487   cruise measurements. **MC, JZ, HT, BL,** and **QS** analyzed the data. **MC, JZ,** and **HT** wrote the paper

488   with contributions from all co-authors.

489

490   *Competing interests.* The authors declare that they have no conflict of interest.

491

Atmospheric
Chemistry
and Physics
Discussions

500 **References**

501 Ackerman, A. S., Kirkpatrick, M. P., Stevens, D. E., and Toon, O. B.: The impact of humidity above

502   stratiform clouds on indirect aerosol climate forcing, Nature, 432, 1014, 2004.

503 Adam, M., Putaud, J. P., Martins dos Santos, S., Dell'Acqua, A., and Gruening, C.: Aerosol

504   hygroscopicity at a regional background site (Ispra) in Northern Italy, Atmos. Chem. Phys., 12,

505   5703-5717, 2012.

506 Atwood, S. A., Reid, J. S., Kreidenweis, S. M., Blake, D. R., Jonsson, H. H., Lagrosas, N. D., Xian, P.,

507   Reid, E. A., Sessions, W. R., and Simpas, J. B.: Size-resolved aerosol and cloud condensation nuclei

508   (CCN) properties in the remote marine South China Sea – Part 1: Observations and source

509   classification, Atmos. Chem. Phys., 17, 1105-1123, 2017.

510 Berg, O. H., Swietlicki, E., and Krejci, R.: Hygroscopic growth of aerosol particles in the marine

511   boundary layer over the Pacific and Southern Oceans during the First Aerosol Characterization

512   Experiment (ACE 1), J. Geophys. Res.-Atmos., 103, 16535-16545, 1998.

513 Cai, M., Tan, H., Chan, C. K., Mochida, M., Hatakeyama, S., Kondo, Y., Schurman, M. I., Xu, H., Li,

514   F., and Shimada, K.: Comparison of Aerosol Hygroscopcity, Volatility, and Chemical Composition

515   between a Suburban Site in the Pearl River Delta Region and a Marine Site in Okinawa, Aerosol Air

516   Qual. Res., 2017.

517 Cai, M., Tan, H., Chan, C. K., Qin, Y., Xu, H., Li, F., Schurman, M. I., Li, L., and Zhao, J.: The size

518   resolved cloud condensation nuclei (CCN) activity and its prediction based on aerosol

519   hygroscopicity and composition in the Pearl Delta River (PRD) Region during wintertime 2014,

520   Atmos. Chem. Phys., 18, 16419-16437, 2018.

521 Cerully, K., Raatikainen, T., Lance, S., Tkacik, D., Tiitta, P., Petäjä, T., Ehn, M., Kulmala, M., Worsnop,

Atmospheric
Chemistry
and Physics
Discussions

522   D., and Laaksonen, A.: Aerosol hygroscopicity and CCN activation kinetics in a boreal forest

523   environment during the 2007 EUCAARI campaign, Atmos. Chem. Phys., 11, 12369-12386, 2011.

524   Choi, Y., and Ghim, Y. S.: Assessment of the clear-sky bias issue using continuous PM10 data from two

525   AERONET sites in Korea, J. Environ. Sci., 53, 151-160, 2017.

526   Chuang, M.-T., Chang, S.-C., Lin, N.-H., Wang, J.-L., Sheu, G.-R., Chang, Y.-J., and Lee, C.-T.:

527   Aerosol chemical properties and related pollutants measured in Dongsha Island in the northern

528   South China Sea during 7-SEAS/Dongsha Experiment, Atmos. Environ., 78, 82-92, 4, 2013.

529   Durkee, P. A., Jensen, D., Hindman, E., and Haar, T.: The relationship between marine aerosol particles

530   and satellite‐detected radiance, J. Geophys. Res.-Atmos., 91, 4063-4072, 1986.

531   Feng, Y., Wang, A., Wu, D., and Xu, X.: The influence of tropical cyclone Melor on PM10

532   concentrations during an aerosol episode over the Pearl River Delta region of China: Numerical

533   modeling versus observational analysis, Atmos. Environ., 41, 4349-4365, 2007.

534   Fröhlich, R., Cubison, M. J., Slowik, J. G., Bukowiecki, N., Prévôt, A. S. H., Baltensperger, U.,

535   Schneider, J., Kimmel, J. R., Gonin, M., and Rohner, U.: The ToF-ACSM: a portable aerosol

536   chemical speciation monitor with TOFMS detection, Atmos. Meas. Tech., 6, 3225-3241, 2013.

537   Hersey, S., Sorooshian, A., Murphy, S., Flagan, R., and Seinfeld, J.: Aerosol hygroscopicity in the

538   marine atmosphere: A closure study using high-time-resolution, multiple-RH DASH-SP and

539   size-resolved C-ToF-AMS data, Atmos. Chem. Phys., 9, 2543-2554, 2009.

540   Hong, J., Häkkinen, S. A. K., Paramonov, M., Äijälä, M., Hakala, J., Nieminen, T., Mikkilä, J., Prisle,

541   N. L., Kulmala, M., and Riipinen, I.: Hygroscopicity, CCN and volatility properties of submicron

542   atmospheric aerosol in a boreal forest environment during the summer of 2010, Atmos. Chem.

543   Phys., 14, 29097-29136, 2014.

Atmospheric
Chemistry
and Physics
Discussions

544   Huang, R.., Zhang, Y., Bozzetti, C., Ho, K.-F., Cao, J.-J., Han, Y., Daellenbach, K. R., Slowik, J. G.,

545   Platt, S. M., and Canonaco, F.: High secondary aerosol contribution to particulate pollution during

546   haze events in China, Nature, 514, 218, 2014.

547   Huang, S., Wu, Z., Poulain, L., Pinxteren, M. V., Merkel, M., Assmann, D., Herrmann, H., and

548   Wiedensohler, A.: Source apportionment of the submicron organic aerosols over the Atlantic Ocean

549   from 53 °N to 53 °S using HR-ToF-AMS, Atmos. Chem. Phys., 1-35, 2018.

550   John, V. O., Holl, G., Allan, R. P., Buehler, S. A., Parker, D. E., and Soden, B. J.: Clear‑sky biases in

551   satellite infrared estimates of upper tropospheric humidity and its trends, J. Geophys. Res.-Atmos.,

552   116, D14108, doi:10.1029/2010JD015355, 2011.

553   Johnson, B., Shine, K., and Forster, P.: The semi‑direct aerosol effect: Impact of absorbing aerosols

554   on marine stratocumulus, Q. J. Roy. Meteor. Soc., 130, 1407-1422, 2004.

555   Köhler, H.: The nucleus in and the growth of hygroscopic droplets, T. Faraday Soc., 32, 1152-1161,

556   1936.

557   Kim, J. H., Yum, S. S., Lee, Y. G., and Choi, B. C.: Ship measurements of submicron aerosol size

558   distributions over the Yellow Sea and the East China Sea, Atmos. Res., 93, 700-714, 2009.

559   Kleidman, R. G., O'Neill, N. T., Remer, L. A., Kaufman, Y. J., Eck, T. F., Tanré, D., Dubovik, O., and

560   Holben, B. N.: Comparison of Moderate Resolution Imaging Spectroradiometer (MODIS) and

561   Aerosol Robotic Network (AERONET) remote-sensing retrievals of aerosol fine mode fraction

562   over ocean, J. Geophys. Res.-Atmos., 110, D22205, doi:10.1029/2005JD005760, 2005.

563   Lehahn, Y., Koren, I., Boss, E., Ben-Ami, Y., and Altaratz, O.: Estimating the maritime component of

564   aerosol optical depth and its dependency on surface wind speed using satellite data, Atmos. Chem.

565   Phys., 10, 6711-6720, 2010.

Atmospheric
Chemistry
and Physics
Discussions

566   Liu, H. J., Zhao, C. S., Nekat, B., Ma, N., Wiedensohler, A., van Pinxteren, D., Spindler, G., Müller, K.,

567   and Herrmann, H.: Aerosol hygroscopicity derived from size-segregated chemical composition and

568   its parameterization in the North China Plain, Atmos. Chem. Phys., 14, 2525-2539, 2014.

569   Lv, Z., Liu, H., Ying, Q., Fu, M., Meng, Z., Wang, Y., Wei, W., Gong, H., and He, K.: Impacts of

570   shipping emissions on PM2.5 pollution in China, Atmos. Chem. Phys., 18, 15811–15824, 2018.

571   Moore, R. H., Nenes, A., and Medina, J.: Scanning Mobility CCN Analysis—A Method for Fast

572   Measurements of Size-Resolved CCN Distributions and Activation Kinetics, Aerosol Sci. Tech., 44,

573   861-871, 2010.

574   Mulcahy, J., O'Dowd, C., Jennings, S., and Ceburnis, D.: Significant enhancement of aerosol optical

575   depth in marine air under high wind conditions, Geophys. Res. Let., 35, L16810,

576   doi:10.1029/2008GL034303, 2008.

577   Ovadnevaite, J., Ceburnis, D., Leinert, S., Dall'Osto, M., Canagaratna, M., O'Doherty, S., Berresheim,

578   H., and O'Dowd, C.: Submicron NE Atlantic marine aerosol chemical composition and abundance:

579   Seasonal trends and air mass categorization, Journal of Geophysical Research: Atmospheres, 119,

580   11,850-811,863, 2014.

581   Petters, M., and Kreidenweis, S.: A single parameter representation of hygroscopic growth and cloud

582   condensation nucleus activity, Atmos. Chem. Phys., 7, 1961-1971, 2007.

583   Pierce, J., Leaitch, W., Liggio, J., Westervelt, D., Wainwright, C., Abbatt, J., Ahlm, L., Al-Basheer, W.,

584   Cziczo, D., and Hayden, K.: Nucleation and condensational growth to CCN sizes during a sustained

585   pristine biogenic SOA event in a forested mountain valley, Atmos. Chem. Phys., 12, 3147-3163,

586   2012.

587   Reid, J. S., Hyer, E. J., Johnson, R. S., Holben, B. N., Yokelson, R. J., Zhang, J., Campbell, J. R.,

588   Christopher, S. A., Di Girolamo, L., and Giglio, L.: Observing and understanding the Southeast

589   Asian aerosol system by remote sensing: An initial review and analysis for the Seven Southeast

590   Asian Studies (7SEAS) program, Atmos. Res., 122, 403-468, 2013.

591   Reid, J. S., Lagrosas, N. D., Jonsson, H. H., Reid, E. A., Sessions, W. R., Simpas, J. B., Uy, S. N., Boyd,

592   T., Atwood, S. A., and Blake, D. R.: Observations of the temporal variability in aerosol properties

593   and their relationships to meteorology in the summer monsoonal South China Sea/East Sea: the

594   scale-dependent role of monsoonal flows, the Madden–Julian Oscillation, tropical cyclones, squall

595   lines and cold pools, Atmospheric Chemistry and Physics, 15, 1745-1768, 2015.

596   Rose, D., Nowak, A., Achtert, P., Wiedensohler, A., Hu, M., Shao, M., Zhang, Y., Andreae, M. O., and

597   Pöschl, U.: Cloud condensation nuclei in polluted air and biomass burning smoke near the

598   mega-city Guangzhou, China – Part 1: Size-resolved measurements and implications for the

599   modeling of aerosol particle hygroscopicity and CCN activity, Atmos. Chem. Phys., 10, 3365-3383,

600   2010.

601   Tan, H., Yin, Y., Gu, X., Li, F., Chan, P. W., Xu, H., Deng, X., and Wan, Q.: An observational study of

602   the hygroscopic properties of aerosols over the Pearl River Delta region, Atmos. Environ., 77,

603   817-826, 2013.

604   Wang, J., Cubison, M., Aiken, A., Jimenez, J., and Collins, D.: The importance of aerosol mixing state

605   and size-resolved composition on CCN concentration and the variation of the importance with

606   atmospheric aging of aerosols, Atmos. Chem. Phys., 10, 7267-7283, 2010.

607   Wu, Z. J., Poulain, L., Henning, S., Dieckmann, K., Birmili, W., Merkel, M., van Pinxteren, D.,

608   Spindler, G., Müller, K., Stratmann, F., Herrmann, H., and Wiedensohler, A.: Relating particle

609   hygroscopicity and CCN activity to chemical composition during the HCCT-2010 field campaign,

610   Atmos. Chem. Phys., 13, 7983-7996, 2013.

611   Yu, F., and Luo, G.: Simulation of particle size distribution with a global aerosol model: contribution of

612   nucleation to aerosol and CCN number concentrations, Atmos. Chem. Phys., 9, 7691-7710,

613   10.5194/acp-9-7691-2009, 2009.

614   Zhang, M., Wang, Y., Ma, Y., Wang, L., Gong, W., and Liu, B.: Spatial distribution and temporal

615   variation of aerosol optical depth and radiative effect in South China and its adjacent area, Atmos.

616   Environ., 188, 120-128, 2018.

617   Zhang, X., Zhuang, G., Guo, J., Yin, K., and Zhang, P.: Characterization of aerosol over the Northern

618   South China Sea during two cruises in 2003, Atmospheric Environment, 41, 7821-7836, 2007.

619

620 **Table 1.** Summary of the instruments used in the campaign.

Instruments	Parameters
ToF-ACSM	NR-PM$_1$
SMPS+CCNc	PNSD (9-415 nm), Size-resolved CCN Activation Ratio (at SS=0.18%, 0.34%, and 0.59%)
CO Monitor	CO concentration
SO$_2$ Monitor	SO$_2$ concentration
O$_3$ Monitor	O$_3$ concentration
NO$_x$ Monitor	NO$_x$, NO, NO$_2$ concentration

621

622

623 **Table 2.** Summary of average N_{CCN}, D_{50}, and $N_{CCN}/N_{CN,tot}$ at 0.18%, 0.34%, and 0.59% SS during P1,

624 C1, C2, and P2.

Period	SS	0.18%	0.34%	0.59%
P1	N_{CCN} (# cm^{-3})	1824.5	3969.4	7197.7
	D_{50} (nm)	131.5	95.6	65.26
	$N_{CCN}/N_{CN,tot}$	0.19	0.34	0.49
C1	N_{CCN} (# cm^{-3})	565.7	978.3	1329.6
	D_{50} (nm)	105.1	67.2	48.5
	$N_{CCN}/N_{CN,tot}$	0.31	0.54	0.71
C2	N_{CCN} (# cm^{-3})	535.6	844.47	1183.4
	D_{50} (nm)	107.5	68.1	47.8
	$N_{CCN}/N_{CN,tot}$	0.32	0.55	0.73
P2	N_{CCN} (# cm^{-3})	4969.1	7139.6	8679.0
	D_{50} (nm)	100.6	64.8	48.6
	$N_{CCN}/N_{CN,tot}$	0.49	0.74	0.85

625

626

Atmospheric
Chemistry
and Physics
Discussions

627   FIGURE CAPTIONS

628   Figure 1. Ship track and tropical storm Bebinca track during the campaign (a), and schematic diagram

629   of the vessel showing the location of the sea container which housed the onboard instruments during

630   the campaign (b).

631   Figure 2. Temporal profiles of the meausred particle number size distribution (a), mass concentration (b)

632   and mass fraction (c) of chemical composition, N_{CCN} and N_{CN} (d) and the daily averaged κ values with

633   the upper and lower error bars (e). No data were shown between 6th and 8th August due to the

634   instrumental failure of the TOF-ACSM

635   Figure 3. The median and interquartile κ values measured over South China Sea, at urban Guangzhou

636   site, at marine background Okinawa site, and the mean and standard deviation κ values measured over

637   remote South China Sea and at mountain Goldlauter site. The κ values over South China Sea were

638   obtained from CCNc measurements (SS=0.18%, 0.34%, and 0.59%, in blue). The κ values in urban

639   Guangzhou were obtained from CCNc (SS =0.1%, 0.2%, 0.4%, and 0.7%, in orange) and HTDMA

640   measurements (in purple). The κ values in marine region Okinawa were obtained from HTDMA

641   measurements (in green). The κ values in remote South China Sea were obtained from CCNc (SS

642   =0.14% and 0.38%, in orange). The κ values in mountain Goldlauter site were obtained from CCNc

643   (SS =0.07%, 0.10%, 0.19% and 0.38%, in black).

644   Figure 4. Concentrations of SO_2 (a), O_3 (b), CO(c), NO_X (d), N_{CN} (e), N_{CCN} (f), $N_{CCN}/N_{CN,tot}$ at 0.34%

645   SS (g), and κ at 0.34% SS (h) as a function of latitude. The data points were color-coded according to

646   date.

647   Figure 5. Correlations of SO_2 (a), CO (b), NO_X (c), N_{CCN} (d), AR at 0.34% SS (e), and κ at 0.34% SS (f)

648   with N_{CN}. The data were plotted according to color-coded dates.

649   Figure 6. The ship track during P1, C1, C2 and P2 periods

650   Figure 7. The 72 h backward trajectories arriving at the location of the vessel with three heights (150 m,

651   500 m, and 1000 m) during P1 , during C1, during C2 , and during P2 respectively.

652   Figure 8. The average mass fraction of NR-PM$_1$ composition during the C1, C2 and P2 periods

653   Figure 9. The average and standard deviation (shaded area) PNSD, along with trimodal lognormal

654   fitted modes (dash color lines). The average N_{CN} during each period and the parameter μ of each

655   lognormal fit were shown.

656

657
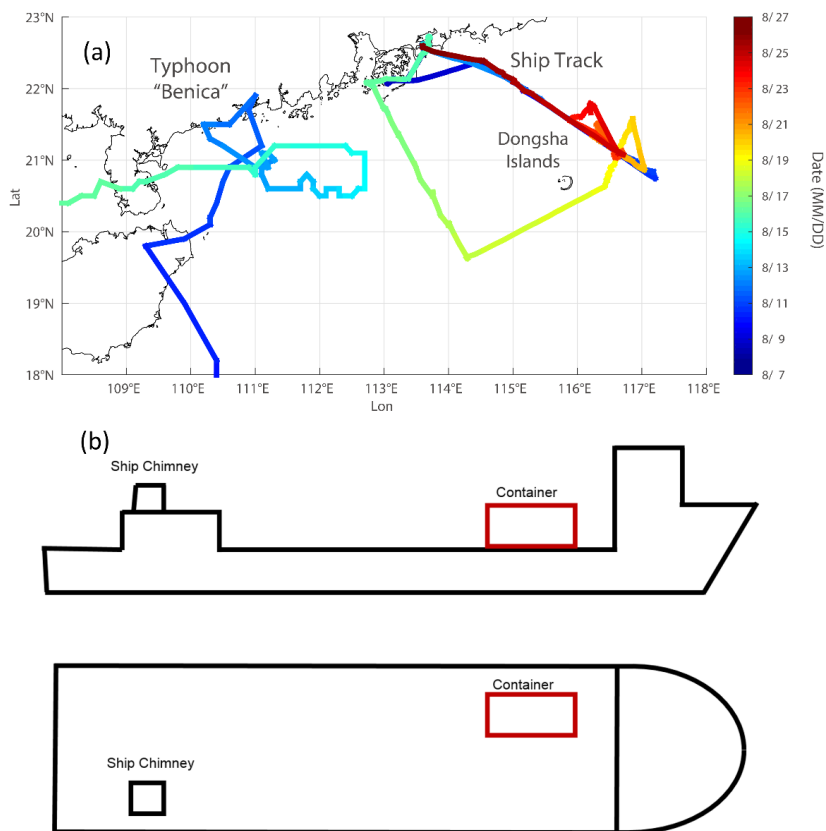
658

659   Fig. 1.

660

661

662

663   Fig. 2.

664

Atmospheric
Chemistry
and Physics

Open Access

EGU

Discussions

665

666

667   Fig. 3.

668

Atmospheric
Chemistry
and Physics
Discussions
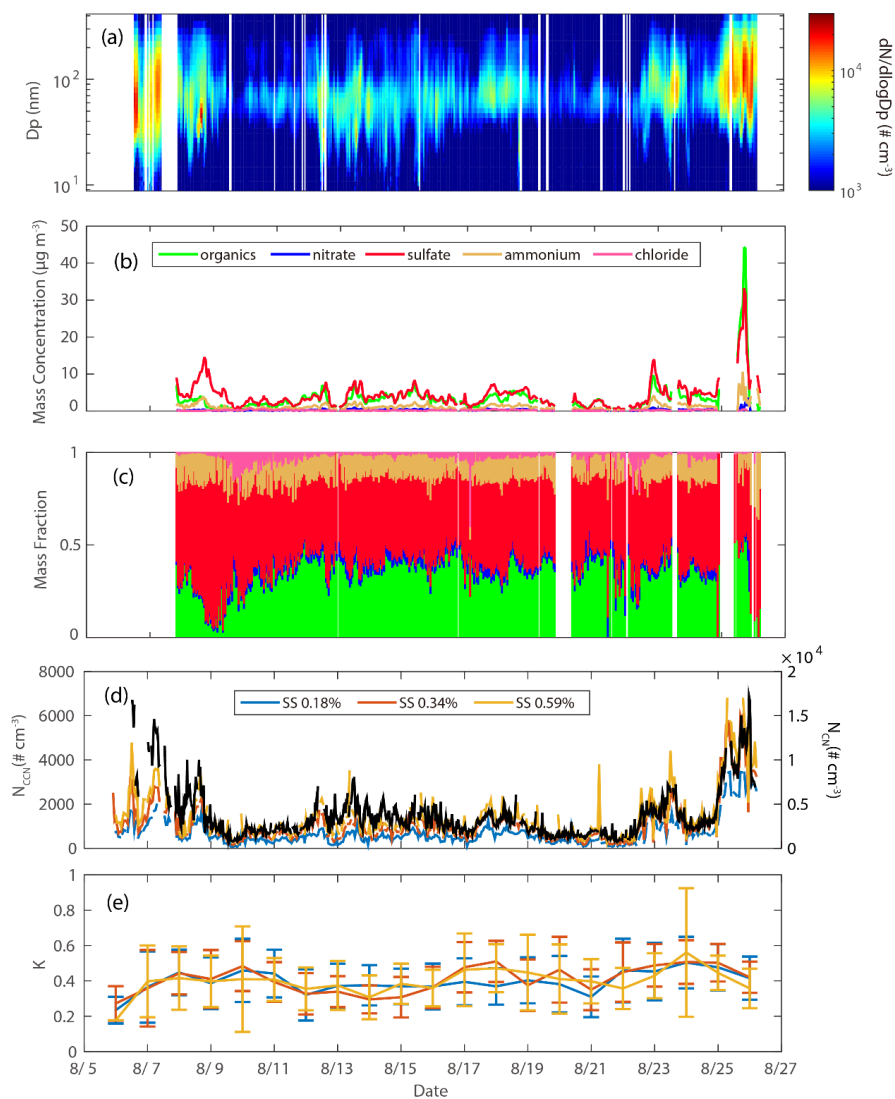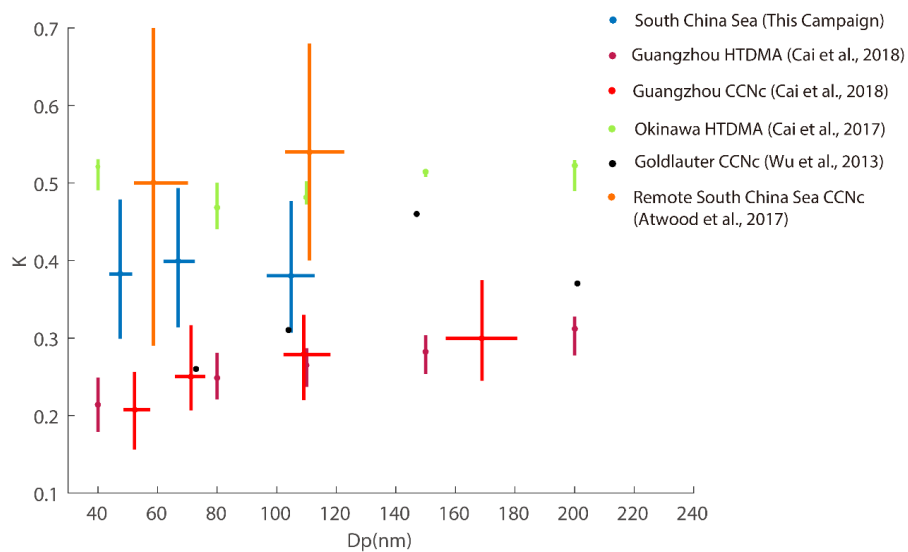
669
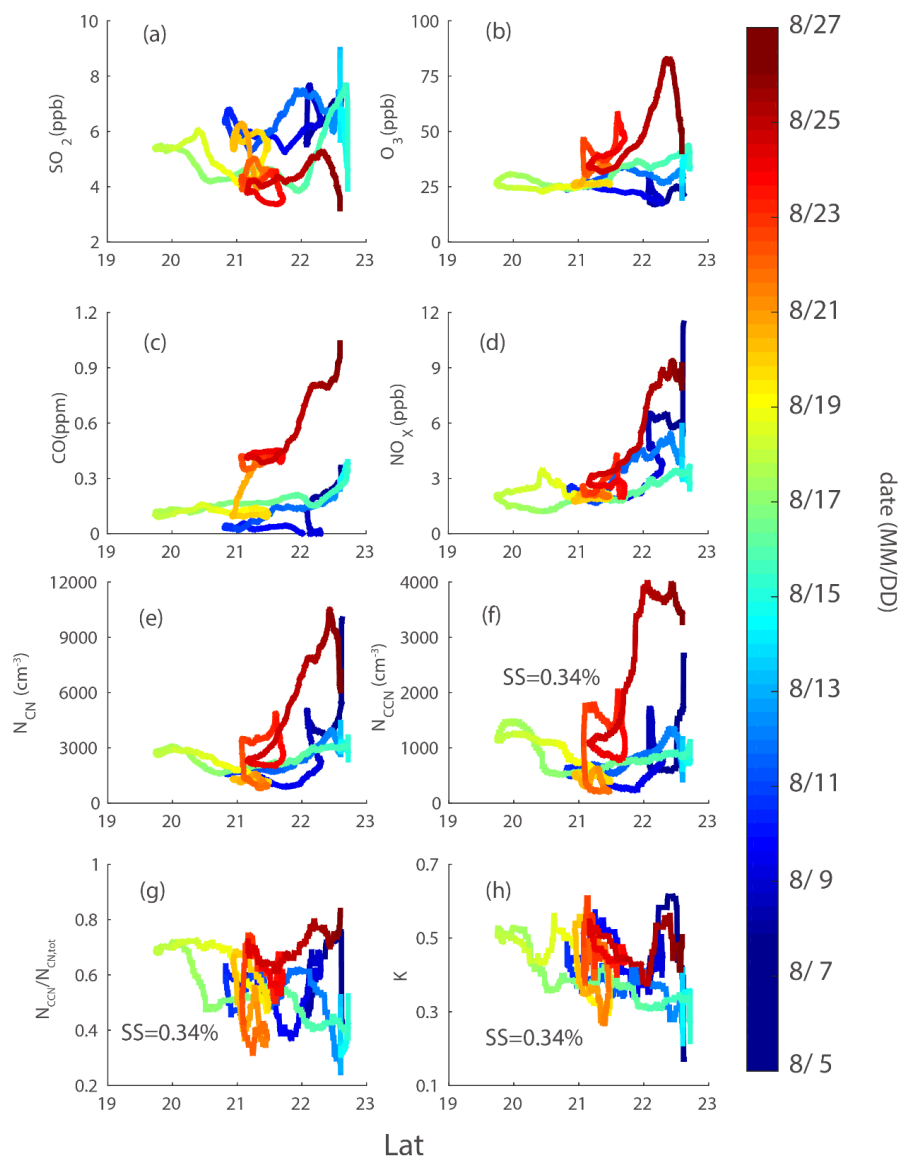
670

671   Fig. 4.

672

673

674

675

676

677   Fig. 5.

678
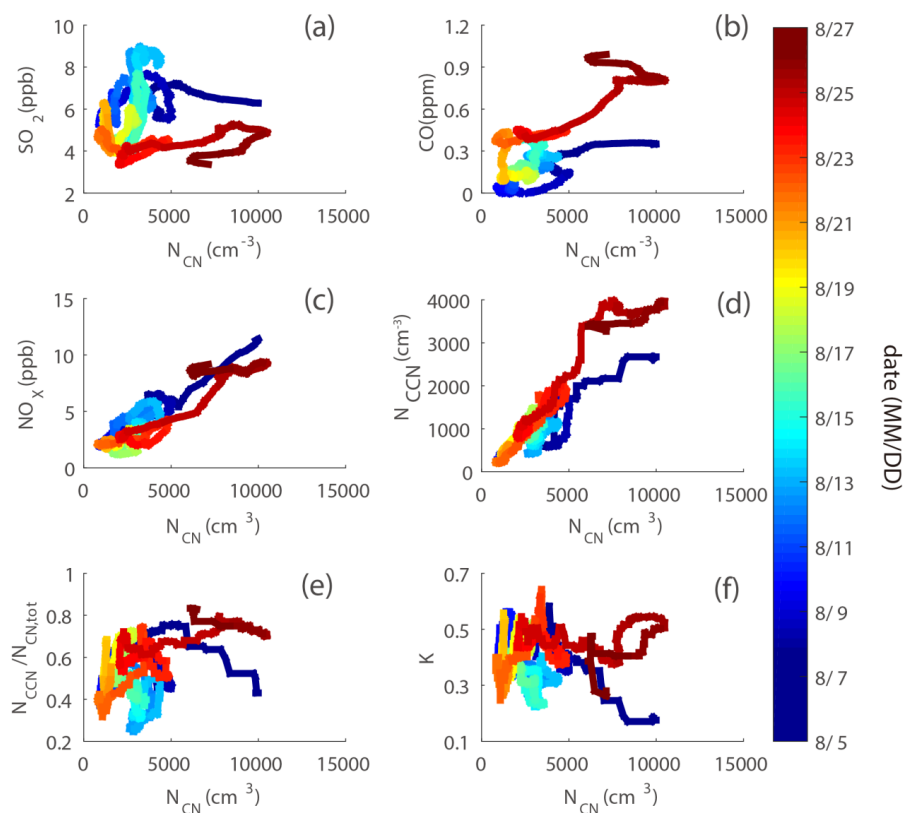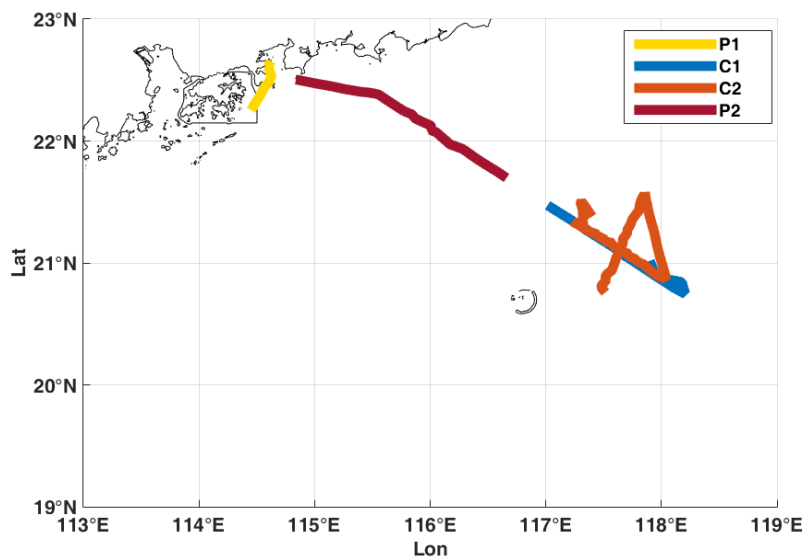
679

680

681   Fig. 6.

682
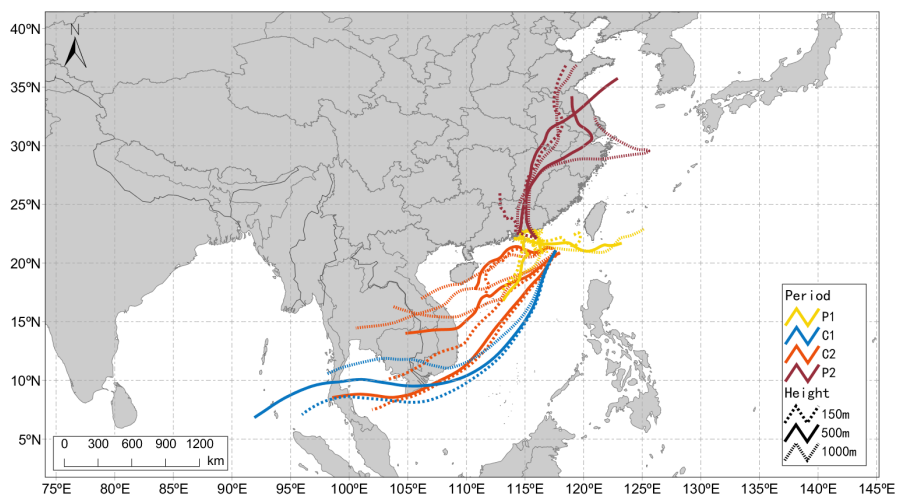
683

684

685   Fig. 7.

686
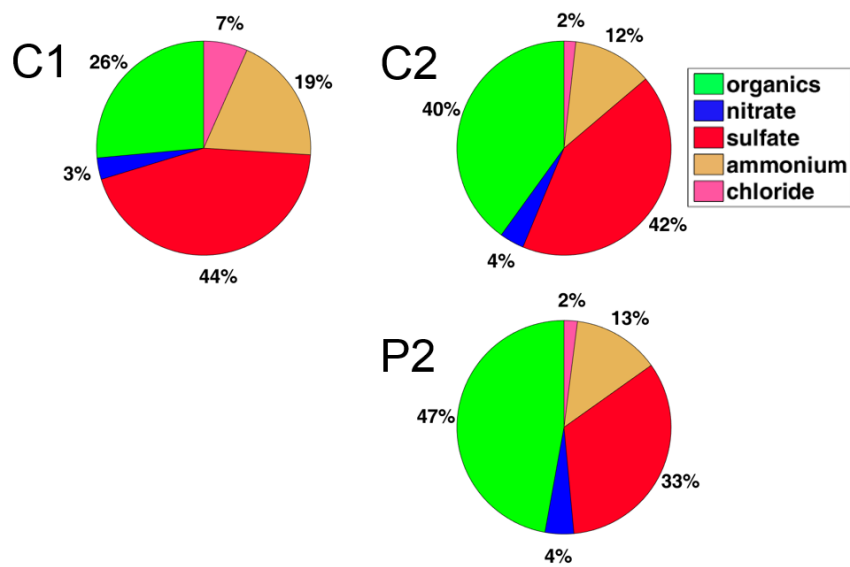
687

688

689   Fig. 8.

690

691

692

693   Fig. 9.

694